

Planar Hall Effect in Antiferromagnetic MnTe Thin Films

Gen Yin,^{1,*†} Jie-Xiang Yu,^{2,*} Yizhou Liu,^{3,4} Roger K. Lake,⁴ Jiadong Zang,^{2,‡} and Kang L. Wang^{1,5,§}

¹Department of Electrical and Computer Engineering, University of California–Los Angeles, Los Angeles, California 90095, USA

²Department of Physics and Materials Science Program, University of New Hampshire, Durham, New Hampshire 03824, USA

³Institute of Physics, Chinese Academy of Sciences, Beijing 100190, China

⁴Laboratory for Terascale and Terahertz Electronics (LATTE), Department of Electrical and Computer Engineering, University of California–Riverside, Riverside, California 92521, USA

⁵Department of Physics and Astronomy, University of California–Los Angeles, Los Angeles, California 90095, USA



(Received 30 May 2018; revised manuscript received 10 January 2019; published 13 March 2019)

We show that the spin-orbit coupling (SOC) in α -MnTe impacts the transport behavior by generating an anisotropic valence-band splitting, resulting in four spin-polarized pockets near Γ . A minimal $k \cdot p$ model is constructed to capture this splitting by group theory analysis, a tight-binding model, and *ab initio* calculations. The model is shown to describe the rotation symmetry of the zero-field planar Hall effect (PHE). The PHE originates from the band anisotropy given by SOC, and is quantitatively estimated to be 25%–31% for an ideal thin film with a single antiferromagnetic domain.

DOI: [10.1103/PhysRevLett.122.106602](https://doi.org/10.1103/PhysRevLett.122.106602)

Antiferromagnets (AFMs) have been considered as a promising candidate for next-generation spintronic devices due to their scalability, their robustness against external magnetic fields, and their ultrafast spin dynamics [1–7]. Without a net magnetization, conventional means to detect and manipulate a ferromagnetic order usually cannot be directly employed in AFMs, which hinders their device applications. Recently, spin-orbit coupling (SOC) was experimentally shown to enable the detection and manipulation of the Néel-vector orientation in easy-plane AFMs [8–11], and therefore became the centerpiece of antiferromagnetic spintronics. SOC is known to induce spin mixing and band splitting, leading to unique magnetotransport signatures. The locking between electron spin and momentum under SOC results in uniform spin accumulation: the spin-galvanic effect [12]. This effect in some antiferromagnets has been shown to exert opposite spin-orbital torques on antiparallel local spins, and thereby switches the Néel vector [8,10,11].

SOC can also lead to anisotropic magnetoresistance (AMR) and the planar Hall effect (PHE) [13–18]. In ferromagnetic transition metals and alloys, PHE is known to result from the s - d mixing given by SOC [14,19]. Although the exact outcome of SOC is strongly material dependent, AMR and PHE are usually proportional to $(\mathbf{M} \cdot \mathbf{j})^2$, and therefore occur in both ferromagnets (FMs) and AFMs [1]. These effects have been experimentally demonstrated in many metallic and semiconducting AFMs, and are considered as a robust method to read out the information encoded in the antiferromagnetic order [8,10,11,20].

Among many AFMs, α -MnTe is particularly attractive both in terms of fundamental physics and device applications [21]. Bulk α -MnTe is a p -type semiconductor with a

Néel temperature of $T_N \approx 310$ K [22–25]. Because of the semiconducting nature, it is convenient to engineer the band alignment and the position of the Fermi level. The Néel vector has three coplanar easy axes, which can naturally encode three-state digital information [23]. In the case of multidomain, the most populated Néel-vector direction can be easily rotated by either field cooling or an applied magnetic field as small as 3 T [9]. These advantages make α -MnTe an attractive candidate material and a convenient building block for antiferromagnetic devices and other related studies.

In this Letter, we seek to theoretically understand the SOC in α -MnTe, and to construct a minimal model that captures the magnetotransport behavior in the case of a thin film. The zero-field PHE is shown to originate from the valence-band anisotropy near Γ induced by SOC. The PHE percentage is shown to maximize above the band crossing, and is estimated to be 25%–31% by a semiclassical transport calculation based on *ab initio* bands.

The ground-state magnetic order of α -MnTe and the band structure are captured by first-principles calculations. α -MnTe has a typical NiAs atomic structure as shown in Figs. 1(a) and 1(b). The lattice constant is relaxed to $a_{1,2} = 4.090$ and $a_3 = 6.430$ Å, $\sim 1\%$ smaller than the values observed in x-ray diffraction [9]. We will use the relaxed values for the rest of the Letter. The impact of the lattice constants will be discussed in the Supplemental Material Sec. I [26]. Each Mn atom possesses a local spin moment of $4.40 \mu_B$, indicating $S = \frac{5}{2}$ high spin state, which is consistent with previous studies [24,25,27]. These spins are known to align ferromagnetically within each Mn layer, whereas the layers stack antiferromagnetically along \hat{z} [direction (001)]. The antiferromagnetic phase is found

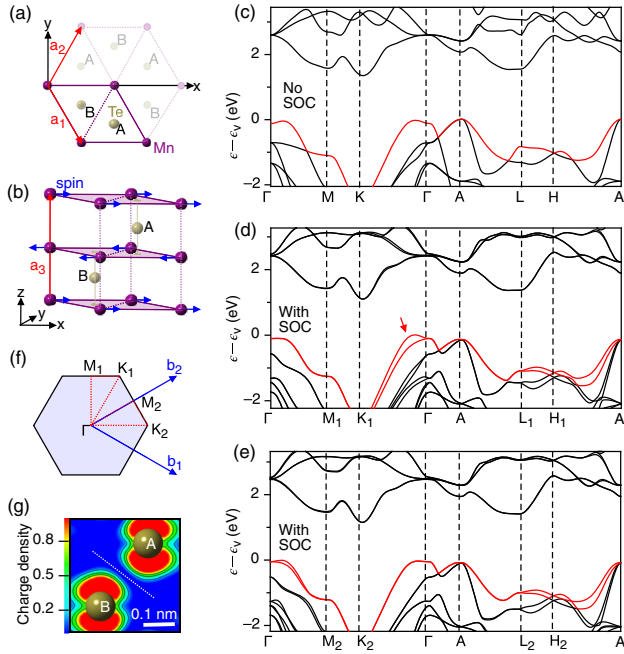


FIG. 1. *Ab initio* band structure for α -MnTe. (a) Top view of the magnetic unit cell and the choice of coordinate. (b) Three-dimensional view of the magnetic unit cell. (c) Electron bands without spin-orbit coupling (SOC), illustrated along the high-symmetry points of the nonmagnetic primitive cell. The red curve denotes the spin-degenerate valence band. (d) and (e) The band structure considering SOC, illustrated along two different loops in the Brillouin zone shown in (f). The red arrow denotes the valence band top near Γ . (g) The charge density contributed by the valence band at Γ . The white dotted line denotes the plane separating the A-Te and B-Te atoms, where the charge density is zero. This color contour plot is illustrated in the plane containing \hat{a}_3 and the two Mn sublattices.

to be 774 meV lower in energy than the ferromagnetic phase, indicating an interlayer antiferromagnetic order as the ground state.

The band structure near the valence band top is strongly affected by SOC. As shown in Figs. 1(c)–1(e), the valence band top is found to be at the A point without SOC, which is ~ 0.05 eV higher than the Γ point. This is consistent with the pioneering calculations done by Podgórny *et al.* [28] and Wei *et al.* [29]. Once SOC is included, the configuration with in-plane spin along \hat{x} [shown in Fig. 1(b)] or the other two equivalent directions has the lowest energy, suggesting that the easy axes are consistent with the recent experiment [9]. With this magnetic order, C_3 rotation about \hat{z} is no longer a symmetry operation so that the Γ -M-K- Γ paths are not identical. This will be explained in detail by the group-theory analysis later. Two representative paths are chosen to demonstrate the band anisotropy, as shown in Fig. 1(f). The most significant SOC splitting occurs in the valence band near the Γ point, as denoted by the red arrow in Fig. 1(d). This splitting shifts the band top from the A point to the $\Gamma \rightarrow K_1 = (-\frac{1}{3}, \frac{2}{3}, 0)$

~ 0.1 eV higher. Cryogenic magnetotransport therefore should be dominated by this band, which is formed by the antibonding of the p_z orbitals of Te($5p$) sitting on different sublattices, as illustrated by the partial charge density in Fig. 1(g). No band splitting shows up in the conduction band, which is dominated by the empty Mn($3d$) $3z^2 - r^2$ orbital. The above calculations are carried out using project augmented wave pseudopotential (PAW) [30] implemented in VASP [31,32]. The generalized gradient approximation (GGA) in Perdew, Burke, and Ernzerhof (PBE) [33] is used as the exchange-correlation energy for structure optimization, whereas the hybrid functional (HSE06) is applied for the calculation of the total energy. This functional computes the exact Fock energy and is known to avoid underestimation of band gaps in certain systems [34,35]. See Sec. II in Supplemental Material [26] for the comparison between the calculated band structure and experimental data from different sources. The k points are sampled on a Γ -centered $13 \times 13 \times 8$ mesh, and an energy cutoff of 400 eV is used throughout all calculations.

To analytically understand the impact of SOC, a minimal effective Hamiltonian describing the long-wavelength behavior is constructed. The NiAs structure of α -MnTe has the space group $P6_3/mmc$ (No. 194). Therefore, the point-group symmetry should be D_{6h} [36] without considering the magnetic order. However, once an in-plane easy axis is selected by the Mn spin, the C_3 symmetry about \hat{z} is broken, and the point group D_{6h} is reduced to its subgroup D_{2h} . This group contains inversion (I) and three mirror operations with respect to xy , yz , and zx planes, respectively. The combination of inversion and mirror leads to three C_2 operations with respect to the x , y , and z axes, respectively. The double group of D_{2h} has 10 irreducible representations, grouped into 5 pairs with opposite parities. The character table of these representations is shown in the Supplemental Material Sec. III [26]. Since the valence band is formed by the antibonding between two p_z orbitals of Te, basis $|\phi_1\rangle = (1/\sqrt{2})(p_{zA} + p_{zB})|\uparrow\rangle$ and $|\phi_2\rangle = (1/\sqrt{2})(p_{zA} + p_{zB})|\downarrow\rangle$ expand a Γ_5^+ irreducible representation of D_{2h} , where the superscript “+” denotes the even parity.

The effective Hamiltonian in this sub-Hilbert space can be constructed by the theory of invariants [37]. Given $\Gamma_5^+ \times \Gamma_5^+ = \Gamma_1^+ \oplus \Gamma_2^+ \oplus \Gamma_3^+ \oplus \Gamma_4^+$, $\hat{H}(\mathbf{k}) = \sum_{\gamma} a_{\gamma} \sum_{k=1}^{|\Gamma_{\gamma}|} h_k^{\gamma}(\mathbf{k}) (\sum_{i,j=1}^2 C_{ij,k}^{\gamma} |\phi_i\rangle \langle \phi_j|)$, where $h_k^{\gamma}(\mathbf{k})$ and $|\Gamma_{\gamma}|$ are the basis and dimension of representation Γ_{γ} , respectively. Coefficients $\{a_{\gamma}\}$ are free parameters that cannot be dictated from the symmetry analysis. $C_{ij,k}$ are the Clebsh-Gordan (CG) coefficients available in Ref. [38]. The lowest order basis of Γ_2^+ and Γ_4^+ are $k_z k_x$ and $k_y k_z$, respectively. Because we are focusing on the transport signature in MnTe thin film, the z direction is modeled as a quantum well state, in which $\langle k_z \rangle = 0$ and $\langle k_z^2 \rangle = (n\pi/d)^2 = \text{const}$, where d is the film thickness and n

are integer values labeling different quantum well states. Since the basis above and their higher order representations all contain odd orders of k_z , Γ_2^+ and Γ_4^+ do not contribute. Up to the fourth order of momentum, the relevant basis of Γ_3^+ are $k_x k_y$, $k_x^3 k_y$, $k_x k_y^3$, and $k_x k_y k_z^2$, where again the last term can be combined with the first one, treating k_z^2 as a constant. The CG coefficients are $C_{ij,1}^3 = (\sigma_z)_{ij}$. For Γ_1^+ , the CG coefficients are $C_{ij,1}^1 = I_{ij}$, whose corresponding Hamiltonian is thus spin independent. The magnetic order is now fully included. One should use \mathbf{k}^2 and \mathbf{k}^4 , the basis of the Γ_1^+ representation of D_{6h} instead. Anisotropic spinless dispersion appears since the 6th order of \mathbf{k} , which is neglected. As a result, we have the generic effective Hamiltonian given by

$$\hat{H}(\mathbf{k}) = \frac{k_0^2}{2m} \left[\bar{\mathbf{k}}^2 - \frac{1}{2} \bar{\mathbf{k}}^4 - \sigma_z (\alpha \bar{k}_x \bar{k}_y + \beta_1 \bar{k}_x^3 \bar{k}_y + \beta_2 \bar{k}_y^3 \bar{k}_x) \right], \quad (1)$$

where k_0 , m , α , β_1 , and β_2 are free parameters. The dimensionless momentum $\bar{\mathbf{k}}$ is defined as $\bar{\mathbf{k}} = \mathbf{k}/k_0$, where k_0 sets the length scale. The minus sign of the quartic term is consistent with the first-principles facts that the splitting occurs in the valence band. To reveal the microscopic origin of this effective Hamiltonian, a tight-binding model based on the $5p$ orbitals of Te atoms is established. Each Te atom on the A site is surrounded by 6 B -site nearest neighbors as shown in Figs. 2(a) and 2(b). Twelve localized atomic orbitals are used to describe the degrees of freedom given by two electron spins, two sublattices, and three $p_{x,y,z}$ orbitals. The SOC is included by taking $H^{\text{SO}} = \lambda \mathbf{L} \cdot \mathbf{S}$ as a perturbative term. The effective Hamiltonian is obtained by a canonical transformation, expanding up to the first order of λ . Keeping k to the fourth order, the resulting effective Hamiltonian is consistent with Eq. (1). See Sec. IV in

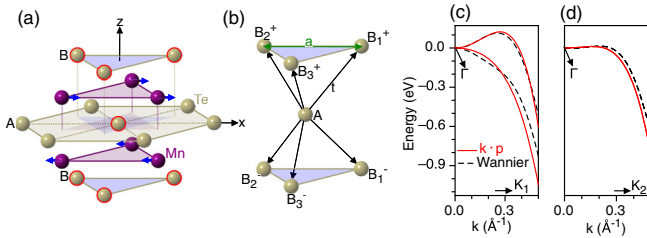


FIG. 2. (a) Atoms that are close to the central Te for a bulk α -MnTe. The red circles label the first-nearest Te atoms used in the tight-binding model. (b) The atomic structure used for the tight-binding model. Each A -site Te is surrounded by six first-nearest B -site ones. (c) and (d) The comparison between the $k \cdot p$ model and the WANNIER model from the *ab initio* calculation. The parameters are $k_0 = 0.162 \text{ \AA}^{-1}$, $\alpha = -6.62$, $\beta_1 = 0.202$, $\beta_2 = 1.191$, and $(k_0^2/2m) = 0.023 \text{ eV}$, as defined in Eq. (1). The comparison is illustrated along the paths $\Gamma \rightarrow K_1$ and $\Gamma \rightarrow K_2$ as denoted in Fig. 1(f).

Supplemental Material [26] for the details of the k_z quantization in thin films; the details of the tight-binding model can be found in Sec. V.

The parameters in Eq. (1) can be obtained by fitting the $k \cdot p$ model to the *ab initio* bands. Here, the fitting target is obtained by transferring the plane-wave basis obtained by VASP into the WANNIER function basis, resulting in a Hamiltonian of localized atomic orbitals (implemented by WANNIER90) [39,40]. The fitting parameters are obtained by machine learning using nonlinear conjugate gradient regression and golden-section line search, minimizing the fitting errors near Γ . See Sec. VI in the Supplemental Material [26] for the details of the machine-learning algorithm. With the optimized parameters, the $k \cdot p$ bands are compared to the *ab initio* bands along $\Gamma \rightarrow K_1$ and $\Gamma \rightarrow K_2$, as shown in Figs. 2(c) and 2(d), respectively. The spin texture of the valence band is shown in Fig. 3(a), where the band edge splits into four pockets polarized along $\pm z$. Importantly, unlike the conventional spin-orbit coupling, the spin-dependent term here is quadratic or quartic in momentum, such that neither time reversal (\mathcal{T}) nor its combination with fractional translation ($\mathcal{T}T_{1/2}$) is a symmetry of the lattice. This therefore leads to nonzero Hall conductivity even in the absence of external magnetic field.

To capture the zero-field PHE, transport behavior induced by the valence-band splitting is studied. Scattering centers induced by vacancies of Mn atoms are considered. Magnetic moments of these impurities point in $\eta \hat{x}$ directions, where $\eta = \pm 1$, denoting two sublattices. The impurity potential is thus written as $\hat{V} = \sum_{\{i,\eta\}} v_0 (a + b\eta\sigma_x) \delta(r - R_{i\eta})$, where $R_{i\eta}$ are positions of magnetic impurities, whereas a and b are spin-independent and spin-dependent scatterings, respectively. The current operator along any direction \hat{n} , $j = \hat{n} \cdot (\partial \hat{H} / \partial \mathbf{k})$, is diagonal so that no interband transition occurs. Intrinsic Berry phase contribution is thus absent. In the diffusive regime with low impurity concentration, the conductivity can be derived by the Kubo-Streda formula

$$\sigma_{\perp(\parallel)}^{\theta_\varepsilon} = \frac{\hbar}{2\pi} \text{Tr} [j_{\parallel}^{\theta_\varepsilon} G^R(\epsilon_F) j_{\perp(\parallel)}^{\theta_\varepsilon} G^A(\epsilon_F)], \quad (2)$$

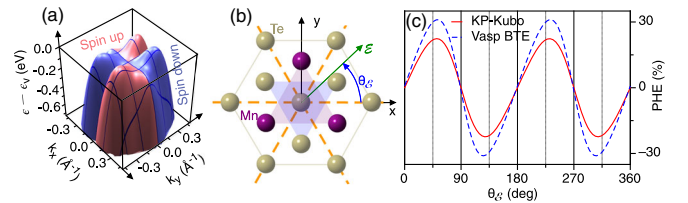


FIG. 3. Planar Hall effect percentage as a function of θ_ε , the angle between the uniform current and the in-plane Néel vector. (a) The full 3D band structure near Γ obtained from the WANNIER model. (b) Illustration of the Néel vector (along \hat{x}), the applied electric field (green arrow) and three in-plane easy axes (orange dashed line). This is a top view of Fig. 2(a). (c) The Hall percentage obtained from transport calculations.

where j_{\parallel} and j_{\perp} are current operators in the parallel and perpendicular directions with respect to the electric field direction, as shown in Fig. 3(b). Given $\theta_{\mathcal{E}}$ as the angle between the electric field \mathcal{E} and \hat{x} , $j_{\parallel}^{\theta_{\mathcal{E}}} = j_x \cos \theta_{\mathcal{E}} + j_y \sin \theta_{\mathcal{E}}$, and $j_{\perp}^{\theta_{\mathcal{E}}} = -j_x \sin \theta_{\mathcal{E}} + j_y \cos \theta_{\mathcal{E}}$. $G^{R,A} = [(G_0^{R,A})^{-1} - \Sigma^{R,A}]^{-1}$ is the retarded (advanced) Green function. In the Born approximation, $\Sigma^{R,A} = \langle \hat{V} \rangle + \langle \hat{V} G^{R,A} \hat{V} \rangle$, where $\langle \dots \rangle$ is the impurity average. Assuming the two Mn sublattices have the same impurity concentration n_i , one obtains $\langle \hat{V} \rangle = 2an_i v_0$, which is just a constant absorbed by the Fermi energy. Therefore, $\Sigma^{R,A} = \mp i/2\tau$, with the relaxation time $\tau^{-1} = \pi^{-1} n_i v_0^2 (a^2 + b^2) \int d^2 \mathbf{q} \delta[\epsilon_F - \epsilon_s(\mathbf{q})]$. Although the Dirac delta function is explicitly spin dependent, the integral over momentum is actually not. This is due to the special band shape: $\epsilon_+(q, \theta) = \epsilon_-(q, -\theta)$. τ is thus spin independent even if $\Sigma^{R,A}$ is solved self-consistently, as will be shown in the Supplemental Material Sec. VII [26]. The PHE percentage is defined by $[\sigma_{\perp}(\theta_{\mathcal{E}})/\sigma_{\parallel}(\theta_{\mathcal{E}})] \times 100\%$, which does not depend on τ , n_i , or v_0 . The numerical result using the $k \cdot p$ model is shown in Fig. 3(c) for $\epsilon_F = \epsilon_V - 0.01$ eV. A major result is the twofold rotational symmetry of the PHE percentage, rather than threefold as suggested by the lattice. This C_2 symmetry originates from the D_{2h} point group brought down from D_{6h} due to the magnetic anisotropy as discussed before. Particularly, both the PHE percentage and the Hall conductivity $\sigma_{\perp}(\theta_{\mathcal{E}})$ are vanishing at $\theta_{\mathcal{E}} = n\pi/2$. At these angles, the mirror reflection about the plane containing \hat{z} and electric field is a symmetry operation, which rules out the Hall effect.

The above transport analysis is based on the minimal $k \cdot p$ model and a constant relaxation time. To show the quantitative accuracy, this result is now compared to the one given by the Boltzmann transport equation (BTE) using the full *ab initio* band. In general, such an effort is necessary to handle the full anisotropic band structure [41,42]. Assuming uniform current distribution and a steady state, BTE is simplified as $-e\mathcal{E} \cdot \nabla_{\mathbf{k}} f = (\partial f / \partial t)|_{\text{coll}}$. Here, $f(\mathbf{k}) = f_0^{\mathbf{k}} + f_1^{\mathbf{k}}$ is the total distribution function, and $f_1^{\mathbf{k}}$ denotes the nonequilibrium part. Assuming $f_1^{\mathbf{k}} = g_{\mathbf{k}} [-(\partial f_0 / \partial \epsilon_F)] \approx g_{\mathbf{k}} \delta(\epsilon - \epsilon_F)$, detailed balance requires $-e\mathcal{E} \cdot \mathbf{v}_{\mathbf{k}} = \sum_{\mathbf{k}'} (g_{\mathbf{k}} - g_{\mathbf{k}'}) S_{\mathbf{k}'\mathbf{k}}$, where $S_{\mathbf{k}'\mathbf{k}}$ is the transition rate from \mathbf{k} to \mathbf{k}' . Here, we consider two types of scattering mechanisms: the spinless Coulomb scattering and the exchange-induced spin-dependent scattering, $\xi = (N_S/N_C)$, which is the concentration ratio between these two types of impurities. Here the transition rate sums over all considered scattering types, $S_{\mathbf{k}'\mathbf{k}} = \sum_{\alpha} S_{\mathbf{k}'\mathbf{k}}^{\alpha}$, where $S_{\mathbf{k}'\mathbf{k}}^{\alpha} = (2\pi N_{\alpha} / \hbar) |H_{\mathbf{k}'\mathbf{k}}^{\alpha}|^2 \delta(\epsilon_{\mathbf{k}} - \epsilon_{\mathbf{k}'})$, and $H_{\mathbf{k}'\mathbf{k}}^{\alpha}$ is the Hamiltonian that scatters \mathbf{k} to \mathbf{k}' . The scattering rate is evaluated between the full-band eigenstates generated by WANNIER90. With a bit algebra, we obtain $g_{\mathbf{k}} = \tau_0^{\mathbf{k}} (\sum_{\mathbf{k}'} S_{\mathbf{k}'\mathbf{k}} g_{\mathbf{k}'} - e\mathcal{E} \cdot \mathbf{v}_{\mathbf{k}'})$, where $\tau_0^{\mathbf{k}} = (\sum_{\mathbf{k}'} S_{\mathbf{k}'\mathbf{k}})^{-1}$. Note that the anisotropy of

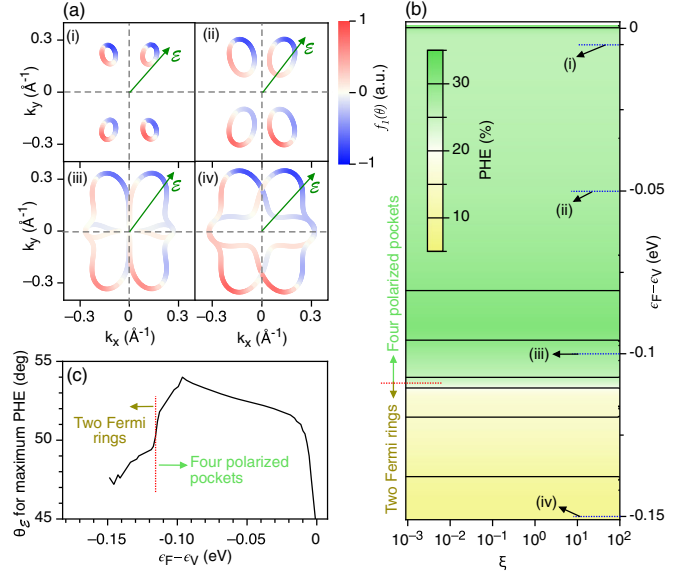


FIG. 4. Full-band Planar Hall effect (PHE) calculated from the Boltzmann equation. (a) The calculated nonequilibrium distribution function $f_{\mathbf{k}}^1$ along different Fermi circles. (b) The PHE percentage as a function of ϵ_F and ξ . Here $\xi = (N_S/N_C)$ is the concentration ratio between spin-polarized and spin-unpolarized scattering centers. (c) The current direction that can maximize PHE percentage for different ϵ_F positions.

transport is fully absorbed by $g_{\mathbf{k}}$ without assuming a constant relaxation time. After discretizing the Brillouin zone with a mesh of 250×250 , $g_{\mathbf{k}}$ can be solved through a linear system. The PHE percentage is defined as $\text{PHE} = (\sum_{\mathbf{k}} f_1^{\mathbf{k}} v_{\perp}^{\mathbf{k}} / \sum_{\mathbf{k}} f_1^{\mathbf{k}} v_{\parallel}^{\mathbf{k}})|_{\epsilon_F} \times 100\%$, which is compared to the $k \cdot p$ result given by Eq. (2) near the valence band edge [Fig. 3(c)]. Both transport models capture a C_2 rotation symmetry instead of C_3 . The solution of $f_1^{\mathbf{k}}$ at four different ϵ_F positions (i)–(iv) are shown in Fig. 4(a). A full scan of ϵ_F and the impurity concentration ratio ξ is then carried out, with the result shown in Fig. 4(b). The PHE percentage is numerically estimated to be 25%–31% above the band crossing. Changing ξ for several orders of magnitude does not change this percentage, suggesting that the ratio between the spin-dependent and independent scattering is not important. This originates from the special band shape $\epsilon_+(q, \theta) = \epsilon_-(q, -\theta)$ as discussed before. Further details of this discussion can be found in Supplemental Material Sec. VIII [26]. The current direction that maximizes PHE [$\theta_{\mathcal{E}}^{\text{max}} = \arg \max_{\theta_{\mathcal{E}}} \text{PHE}(\epsilon_F)$] is shown in Fig. 4(c) for different ϵ_F positions. The value of $\theta_{\mathcal{E}}^{\text{max}}$ varies between 45° – 54° for a wide range of energy, which is determined by the details of the band shape.

The $k \cdot p$ Hamiltonian given by Eq. (1) is not only effective, but also minimal. The quartic spin-orbit coupling term is necessary, in the absence of which, the extra $C_4\mathcal{T}$ symmetry of the quadratic spin-orbit coupling term ($k_x k_y \sigma_z$) rules out the Hall conductivity. The $k_z = 0$

approximation assumes that the transport is dominated by the first subband in a thin film of only a couple of unit cells. It is required to use a full bulk Hamiltonian to capture the crossover from 2D to 3D, which calls for future investigations. The linear-system solution of BTE used above is generic to include arbitrary combinations of elastic scattering mechanisms. This allows for a single-step calculation of the full-band nonequilibrium distribution without requiring self-consistent iterations. The PHE percentage estimated by this calculation is more than 1 order of magnitude greater than that observed in experiments, suggesting a vast space to improve the device performance by engineering the ϵ_F , applying currents along θ_{ξ}^{\max} , or by scaling down the device to the limit of a single antiferromagnetic domain.

The transport analysis and simulations done by G. Y., Y. L., R. L., and K. W. are supported by Spins and Heat in Nanoscale Electronic Systems (SHINES), an EFRC funded by the U.S. Department of Energy (DOE), Office of Science, Basic Energy Sciences (BES) under Award No. SC0012670. J. X. Y. and J. Z. were supported by the U.S. DOE, Office of Science, BES under Award No. DE-SC0016424. First-principles calculations were conducted on Extreme Science and Engineering Discovery Environment (XSEDE) under Grant No. TG-PHY170023, and Trillian, a Cray XE6m-200 supercomputer at UNH supported by the NSF MRI program under Grant No. PHY-1229408. G. Y. and K. W. are also grateful for the support from the National Science Foundation (DMR-1411085), and the ARO program under Contract No. W911NF-15-1-10561.

Note Added in Proof.—It has been pointed out that the detail of the valence band edge is sensitive to the choices of the lattice constants, which are temperature dependent according to early experiments [43]. This might affect the details of the band-edge landscape and the transport behavior. The band structure in this Letter is based on zero-temperature relaxed lattice constants, and the transport analysis is self-consistent in this regime. Detailed study of temperature-dependent behaviors invites further computational and experimental investigations.

*These authors contributed equally to this work.

[†]Corresponding author.

genyin@ucla.edu

[‡]Corresponding author.

jiadong.zang@unh.edu

[§]Corresponding author.

wang@ee.ucla.edu

- [1] V. Baltz, A. Manchon, M. Tsoi, T. Moriyama, T. Ono, and Y. Tserkovnyak, *Rev. Mod. Phys.* **90**, 015005 (2018).
 [2] O. Gomonay, T. Jungwirth, and J. Sinova, *Phys. Status Solidi* **11**, 1700022 (2017).

- [3] E. V. Gomonay and V. M. Loktev, *Low Temp. Phys.* **40**, 17 (2014).
 [4] T. Jungwirth, X. Marti, P. Wadley, and J. Wunderlich, *Nat. Nanotechnol.* **11**, 231 (2016).
 [5] J. Železný, P. Wadley, K. O. A. Hoffmann, and H. Ohno, [arXiv:1705.10675](https://arxiv.org/abs/1705.10675).
 [6] M. B. Jungfleisch, W. Zhang, and A. Hoffmann, *Phys. Lett. A* **382**, 865 (2018).
 [7] J. Železný, P. Wadley, K. Olejník, A. Hoffmann, and H. Ohno, *Nat. Phys.* **14**, 220 (2018).
 [8] P. Wadley, B. Howells, J. Železný, C. Andrews, V. Hills, R. P. Campion, V. Novák, K. Olejník, F. Maccherozzi, S. S. Dhesi *et al.*, *Science* **351**, 587 (2016).
 [9] D. Kriegner, K. Výborný, K. Olejník, H. Reichlová, V. Novák, X. Marti, J. Gazquez, V. Saidl, P. Němec, V. V. Volobuev *et al.*, *Nat. Commun.* **7**, 11623 (2016).
 [10] S. Y. Bodnar, L. Šmejkal, I. Turek, T. Jungwirth, O. Gomonay, J. Sinova, A. A. Sapozhnik, H.-J. Elmers, M. Kläui, and M. Jourdan, *Nat. Commun.* **9**, 348 (2018).
 [11] M. J. Grzybowski, P. Wadley, K. W. Edmonds, R. Beardsley, V. Hills, R. P. Campion, B. L. Gallagher, J. S. Chauhan, V. Novak, T. Jungwirth *et al.*, *Phys. Rev. Lett.* **118**, 057701 (2017).
 [12] S. D. Ganichev, E. L. Ivchenko, V. V. Bel'kov, S. A. Tarasenko, M. Sollinger, D. Weiss, W. Wegscheider, and W. Prettl, *Nature (London)* **417**, 153 (2002).
 [13] W. Thomson, *Proc. R. Soc. London* **8**, 546 (1857).
 [14] J. Smit, *Physica* **17**, 612 (1951).
 [15] T. McGuire and R. Potter, *IEEE Trans. Magn.* **11**, 1018 (1975).
 [16] M. Wu, G. Zheng, W. Chu, W. Gao, H. Zhang, J. Lu, Y. Han, J. Yang, H. Du, W. Ning *et al.*, *Phys. Rev. B* **98**, 161110 (2018).
 [17] S. Nandy, G. Sharma, A. Taraphder, and S. Tewari, *Phys. Rev. Lett.* **119**, 176804 (2017).
 [18] A. A. Burkov, *Phys. Rev. B* **96**, 041110 (2017).
 [19] I. A. Campbell, A. Fert, and O. Jaoul, *J. Phys. C* **3**, S95 (1970).
 [20] T. Jungwirth, J. Sinova, A. Manchon, X. Marti, J. Wunderlich, and C. Felser, *Nat. Phys.* **14**, 200 (2018).
 [21] J. J. Wasscher, *Electrical Transport Phenomena in MnTe, An Antiferromagnetic Semiconductor* (Technische Hogeschool, Eindhoven, 1969).
 [22] J. B. C. Efreem D'Sa, P. A. Bhobe, K. R. Priolkar, A. Das, S. K. Paranjpe, R. B. Prabhu, and P. R. Sarode, *J. Magn. Mater.* **285**, 267 (2005).
 [23] D. Kriegner, H. Reichlova, J. Grenzer, W. Schmidt, E. Ressouche, J. Godinho, T. Wagner, S. Y. Martin, A. B. Shick, V. V. Volobuev *et al.*, *Phys. Rev. B* **96**, 214418 (2017).
 [24] W. Szuszkiewicz, E. Dynowska, B. Witkowska, and B. Hennion, *Phys. Rev. B* **73**, 104403 (2006).
 [25] K. Walther, *Solid State Commun.* **5**, 399 (1967).
 [26] See Supplemental Material at <http://link.aps.org/supplemental/10.1103/PhysRevLett.122.106602> for details of the *ab initio* calculation, the analytical model and the transport calculation.
 [27] M. Krause and F. Bechstedt, *J. Supercond. Novel Magn.* **26**, 1963 (2013).
 [28] M. Podgorny and J. Oleszkiewicz, *J. Phys. C* **16**, 2547 (1983).

- [29] S.-H. Wei and A. Zunger, *Phys. Rev. B* **35**, 2340 (1987).
- [30] P. E. Blöchl, *Phys. Rev. B* **50**, 17953 (1994).
- [31] G. Kresse and J. Furthmüller, *Comput. Mater. Sci.* **6**, 15 (1996).
- [32] G. Kresse and J. Furthmüller, *Phys. Rev. B* **54**, 11169 (1996).
- [33] J. P. Perdew, K. Burke, and M. Ernzerhof, *Phys. Rev. Lett.* **78**, 1396 (1997).
- [34] J. Heyd, G. E. Scuseria, and M. Ernzerhof, *J. Chem. Phys.* **118**, 8207 (2003).
- [35] A. V. Krukau, O. A. Vydrov, A. F. Izmaylov, and G. E. Scuseria, *J. Chem. Phys.* **125**, 224106 (2006).
- [36] L. M. Sandratskii, R. F. Egorov, and A. A. Berdyshev, *Phys. Status Solidi (b)* **104**, 103 (1981).
- [37] R. Winkler, *Spin-Orbit Coupling Effects in Two-Dimensional Electron and Hole Systems*, Springer Tracts in Modern Physics (Springer-Verlag, Berlin Heidelberg, 2003).
- [38] G. F. Koster, *Space Groups and their Representations* (Academic Press, New York, 2012).
- [39] A. A. Mostofi, J. R. Yates, G. Pizzi, Y.-S. Lee, I. Souza, D. Vanderbilt, and N. Marzari, *Comput. Phys. Commun.* **185**, 2309 (2014).
- [40] I. Souza, N. Marzari, and D. Vanderbilt, *Phys. Rev. B* **65**, 035109 (2001).
- [41] K. Výborný, A. A. Kovalev, J. Sinova, and T. Jungwirth, *Phys. Rev. B* **79**, 045427 (2009).
- [42] C. Xiao, D. Li, and Z. Ma, *Phys. Rev. B* **95**, 035426 (2017).
- [43] S. Greenwald, *Acta Cryst.* **6**, 396 (1953).